Available online at www.sciencedirect.com

ScienceDirect

Acta Materialia 58 (2010) 5070–5085

Acta MATERIALIA

www.elsevier.com/locate/actamat

Identification of $MnCr_2O_4$ nano-octahedron in catalysing pitting corrosion of austenitic stainless steels

S.J. Zheng [a], Y.J. Wang [a], B. Zhang [a], Y.L. Zhu [a], C. Liu [a], P. Hu [b], X.L. Ma [a,*]

[a] Shenyang National Laboratory for Materials Science, Institute of Metal Research, Chinese Academy of Sciences, 110016 Shenyang, China
[b] School of Chemistry and Chemical Engineering, The Queen's University Belfast, Belfast BT9 5AG, UK

Received 3 February 2010; received in revised form 29 April 2010; accepted 21 May 2010
Available online 16 June 2010

Abstract

Pitting corrosion of stainless steels, one of the classical problems in materials science and electrochemistry, is generally believed to originate from the local dissolution in MnS inclusions, which are more or less ubiquitous in stainless steels. However, the initial location where MnS dissolution preferentially occurs is known to be unpredictable, which makes pitting corrosion a major concern. In this work we show, at an atomic scale, the initial site where MnS starts to dissolve in the presence of salt water. Using in situ ex-environment transmission electron microscopy (TEM), we found a number of nano-sized octahedral $MnCr_2O_4$ crystals (with a spinel structure and a space group of $Fd\bar{3}m$) embedded in the MnS medium, generating local $MnCr_2O_4$/MnS nano-galvanic cells. The TEM experiments combined with first-principles calculations clarified that the nano-octahedron, enclosed by eight {1 1 1} facets with metal terminations, is "malignant", and this acts as the reactive site and catalyses the dissolution of MnS. This work not only uncovers the origin of MnS dissolution in stainless steels, but also presents an atomic-scale evolution in a material's failure which may occur in a wide range of engineering alloys and biomedical instruments serving in wet environments.

Keywords: Scanning/transmission electron microscopy (STEM); Corrosion; Catalysis; Electrochemistry; Stainless steel

1. Introduction

Stainless steels are widely used for their superior corrosion resistance. However, stainless steels are actually not "stainless"; in the presence of aggressive anionic species they are susceptible to localized pitting corrosion, one of the major causes of the material's failure [1–5]. Great efforts have been made in the past several decades [3–21] to figure out the origin of pitting corrosion and to better control or avoid such a failure process.

In addition to carbon in stainless steels, sulphur also plays a critical role in influencing the material's properties. The sulphur content in stainless steel is designed on the basis of an integrated consideration [22]. Sulphur in stainless steel is usually present in the form of manganese sulphide (MnS), the lubricating effect of which is needed for machining. However, high sulphur content, and therefore high volume of MnS in stainless steels, results in poorer corrosion resistance, since it is generally believed that the pitting event results from the local dissolution [6–15] in MnS inclusion. From the metallurgical point of view, Williams and Zhu [18] proposed that chemical changes in and around MnS inclusions are a mechanism for the pitting initiation. Following this proposal, Ryan et al. [19] carried out a chemical composition analysis by means of secondary ion mass spectroscopic analysis of areas selectively sputtered by a focused ion beam. They reported a significant reduction in the Cr:Fe ratio of the steel matrix around MnS particles, and proposed that the chromium-depleted zones are susceptible to high-rate dissolution that "triggers" pitting [19]. In contrast, Meng et al. [20] failed to find such chromium-depleted zones in the same steel using X-ray energy-dispersive spectroscopy (EDS) analysis under a scanning transmission electron microscope.

---

* Corresponding author. Tel.: +86 24 23971845.
E-mail address: xlma@imr.ac.cn (X.L. Ma).

1359-6454/$36.00 © 2010 Acta Materialia Inc. Published by Elsevier Ltd. All rights reserved.
doi:10.1016/j.actamat.2010.05.043

Although pitting corrosion in stainless steels is confirmed to be associated with MnS inclusion, the link between local chemistry and pitting corrosion has not yet been established because of the lack of information, at an atomic scale, on the initial site where MnS dissolution preferentially occurs. Such a lacking results from the fact that the widely used analytical approaches have been based on scanning electron microscopy [6,11,13–16], atomic force microscopy [11,13] and scanning Auger microscopy [8,10,16], which cannot provide local three-dimensional (3D) information with required spatial/chemical resolution.

Pitting corrosion remains one of the classical problems in the fields of electrochemistry and materials science. To seize the initial site of MnS dissolution and hence pitting corrosion, in situ observation in the presence of chemical medium is needed in order to monitor such a process, and additionally the spatial as well as chemical resolutions in the analytical approach must be high enough up to an atomic level in 3D. In this work, we have applied an in situ ex-environment transmission electron microscopy (TEM) technique combined with the first-principles calculations, and provided atomic-scale information on the initial site where MnS dissolution occurs, which was unknown for decades. The present study is expected to set up a new basis on which the electrochemical theory of pitting corrosion can be established.

2. Experimental procedures

2.1. Sample preparation

A commercial 316F type austenite stainless steel with high sulphur content was chosen as the major object because it contains a large number of MnS inclusions for analysis. In addition, another representative of austenite stainless steels (304-type with relatively lower sulphur content) was studied in this work. These steels were made by Nippon Steel and Sumikin Stainless Steel Corporation, and are used in countless diverse applications. Compositions (in wt.%) of the 316F steel are labelled in Table 1. The as-received stainless steel in the present study was hot-rolled into rods with diameter of 1 cm. Such a rolling made the MnS inclusions needle-shaped, and are parallel to the rolling direction.

2.2. TEM specimen preparation

The steel rod was first cut into sections of 3 mm using a linear precision saw. Pieces parallel to the rolling direction were sliced with the thickness of 300 μm. Disks with diameter of 3 mm were prepared by die-cutting and then ultrasonically cleaned in acetone to remove particles and machine oil, which might stick on their surface during the cutting. The samples were then ground using variant grit silicon carbide papers, polished with diamond paste to 1 μm finish, and finally thinned by ion-milling. After the first-round TEM observation, some of the specimens were plasma-cleaned and then immersed into the 1 M NaCl solution at room temperature for various periods (the duration ranged from 5 to 90 min). The TEM specimens which experienced the corrosion tests were quickly cleaned (in distilled water and methanol), dried, and transferred into the TEM for further investigation. When corrosion tests (60 min in 1 M NaCl solution in this study) were performed on bulk sample of the steel, a Nova 200 NanoLab UHR FEG-SEM/FIB was used for TEM specimen preparation. The focused ion beam (FIB) current was controlled to decrease gradually in order to reduce the possible damage to the specimen surface. The final current density was ~50 pA.

Table 1
Compositions of the 316F stainless steel in the present study.

S	C	Cr	Ni	Mn	Mo	Co	V
0.16	0.04	16.68	10.07	1.60	2.15	0.13	0.09
Ti	Cu	Si	P	Al	Nb	Sn	Fe
<0.005	0.26	0.46	0.030	0.06	0.04	0.001	Balance

2.3. SEM and TEM characterizations

A SUPRA35 field emission scanning electron microscope (SEM) was used to investigate the morphology of MnS inclusions before and after the corrosion tests (in case the corrosion tests were performed on bulk sample). A Tecnai G^2 F30 transmission electron microscope, equipped with a high-angle angular-dark-field (HAADF) detector and X-ray energy-dispersive spectrometer (EDS) systems, was used at 300 kV for electron diffraction, HAADF imaging, high-resolution electron microscopy (HREM) imaging, and composition analysis. The probe size for EDS line-scan is less than 2 nm and the step size about 3 nm. The 3D tomography was carried out on the TEM equipped with a Gatan tomography sample holder, and the data was acquired by the software 3D scanning transmission electron microscopy (STEM) tomography. During the experiment, the tilt angles ranged from −70° to +70°, and the tilt step was 2°.

2.4. Computation details

All calculations were performed with Vienna Ab initio Simulation Package (VASP) [23,24]. The Perdew–Wang (PW91) generalized gradient approximation (GGA) functional [25] was utilized with projector-augmented wave (PAW) method [26] to describe the core-valence electron interaction. We used a plane-wave cutoff energy of 400 eV and applied a $2 \times 2 \times 1$ k-point mesh for the 2×1 supercells (12.15 Å × 6.07 Å) with a vacuum of 12 Å. The surface slab contained 8 layers and half of them were allowed to relax. Structures were optimized until the Hellman–Feynman force on each atom was smaller than 0.05 eV Å^{-1}. The GGA + U method was used to minimize the error of DFT calculations for materials containing Cr

($U = 3.5$) and Mn ($U = 4$) [27]. Lattice constant of the bulk $MnCr_2O_4$ was optimized to be 8.59 Å, close to the experiment value of 8.437 Å [28].

3. Results and discussion

3.1. Inhomogeneous dissolution within a single MnS inclusion

The casting saw materials of stainless steels usually suffer a hot-rolling or cold-rolling before component-making, during which MnS inclusions were deformed to be needle-shaped. Fig. 1a is an SEM image showing the distribution of the needle-liked MnS inclusions in the present steel. The distributions of MnS inclusions were actually viewed from the directions of perpendicular and parallel, respectively, to the rolling direction. It was seen that the needle-shaped MnS inclusions are parallel to the rolling direction. The dimensions of MnS inclusions are typically 20–50 μm in length and 0.3–1.0 μm in width, respectively, which are obtained statistically on several hundred inclusions in the present study.

An in situ ex-environment TEM method was designated, i.e. a fixed TEM specimen before and after immersion for variant durations (several tens of minutes) in 1 M NaCl solution was repeatedly observed in a TEM, and particular attention was paid to local microstructural evolution in a settled MnS inclusion. At this stage of TEM observation we applied the newly developed HAADF technique in the TEM, since HAADF mode provides incoherent images which uses high-angle scattering and leads to strong atomic number (Z) contrast. Therefore the image contrast in such a mode is strongly associated with the local variety of chemical composition and/or thickness contribution [29].

Fig. 1b is an HAADF image showing an MnS inclusion section. Compared with MnS, steel matrix shows brighter contrast due to much more heavy elements (Fe, Cr, Ni, etc.) therein. Fig. 1c is the same section as that in Fig. 1b but suffered the corrosion in 1 M NaCl solution for 45 min. Different from the steel matrix, remarkable dissolution of MnS was found after the specimen was immersed in the solution. It is of great interest to find that the dissolution of MnS is strongly localized: the pit which results from the local dissolution of MnS features a nano-scale undissolved core, the structure/composition of which might be different from that of MnS. In other words, the initial site of MnS dissolution is at the periphery of a nano-particle which was embedded in MnS medium. On the basis of such an initiation at the interface, the dissolution developed into the MnS matrix, and left a pit behind (compare each counterpart area labelled with I, II, III, IV, and V, respectively, in Fig. 1d and e, which shows zoom-in images of the local area in Fig. 1b and c). This dissolution mode is visualized in 3D (Fig. 1f) by translating the contrast in the experimental images (Fig. 1e).

A number of zoom-in images of such particles around which MnS dissolution occurs are displayed in Fig. 2 with the same magnification. These particles show various dimensions and variant geometric projections, but they

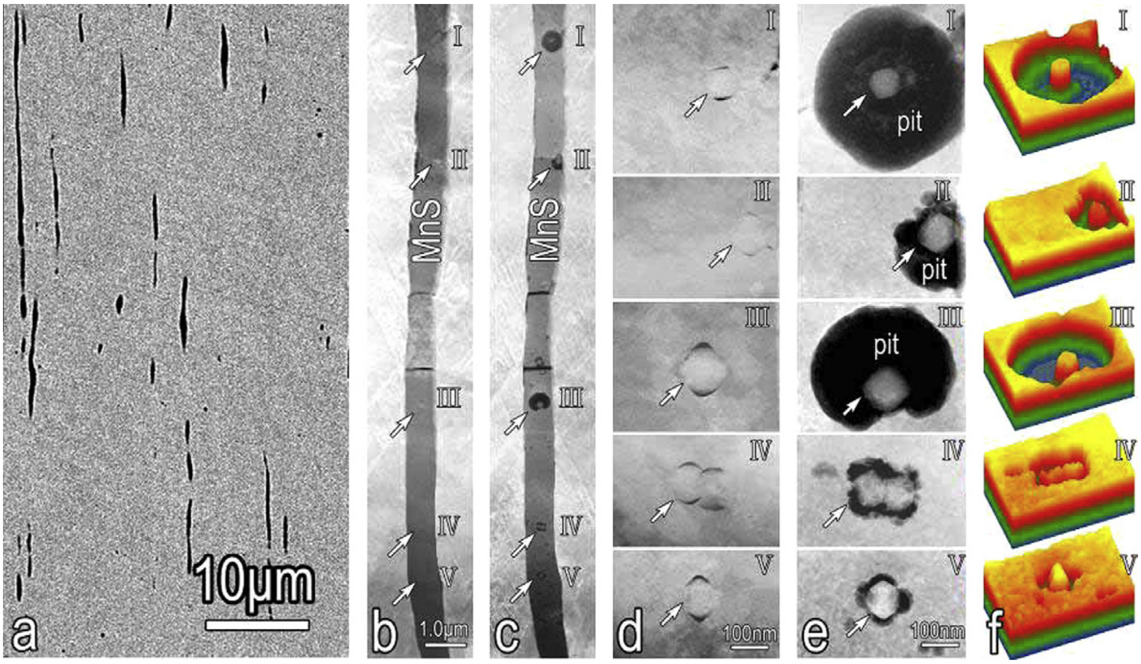

Fig. 1. In situ ex-environment TEM observation showing the localization of inhomogeneous dissolution of MnS in a stainless steel. (a) An SEM image of the as-received 316F stainless steel showing the distribution of needle-like MnS inclusions (in black). (b) An HAADF image showing an MnS inclusion section, in which several nano-particles embedded in MnS are arrowed and labelled. (c) The same section as that in (b) but suffering the corrosion in 1 M NaCl solution for 45 min. The localized dissolution of MnS happened around the particles. (d) Zoom-in images of the nano-particles in (b) labelled with I, II, III, IV, and V. (e) Zoom-in images of the local dissolution around the nano-particles in (c). (f) Dissolution mode visualized by digitizing the contrast in the experimental images in (e).

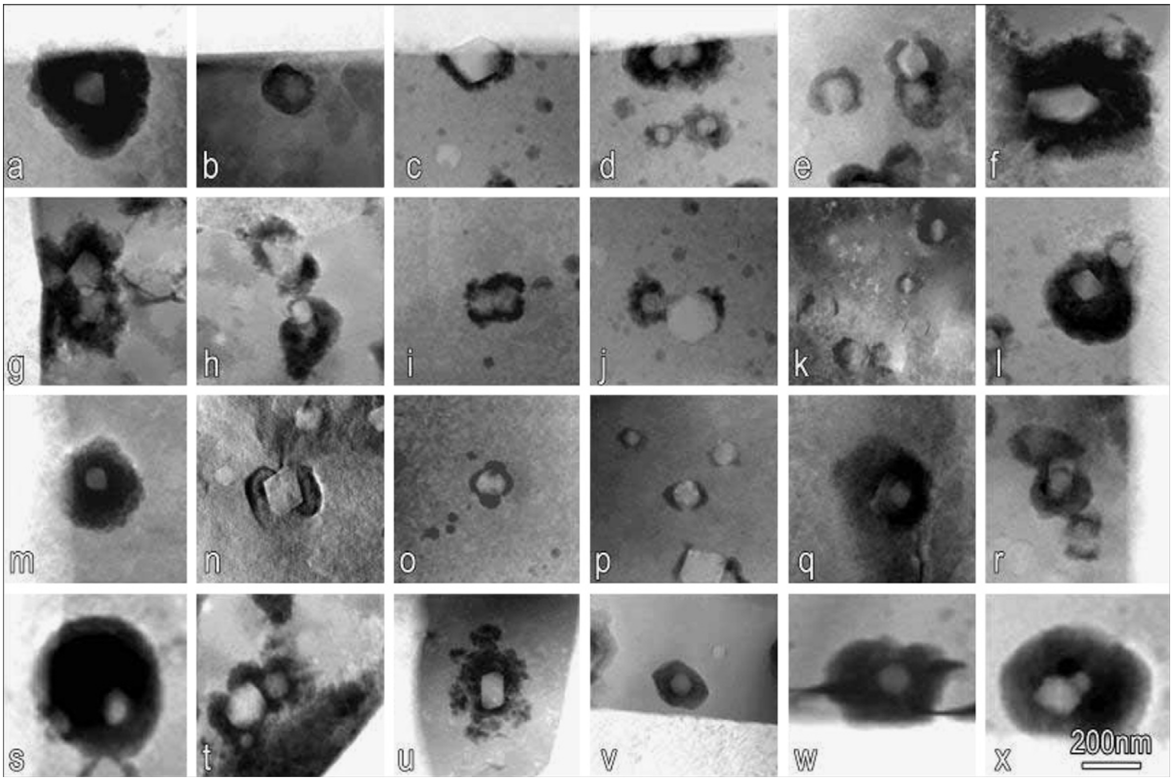

Fig. 2. Zoom-in HAADF images of particles around which MnS dissolution occurred and pits formed. These images are in the same magnification and obtained in the specimens which suffered immersion in NaCl solution for 30–60 min. The pit morphologies around the particles are various. These particles show various dimensions, but they all provide an initial site for MnS dissolution.

all provide initial sites for MnS dissolution, no matter whether they are located at the inner part of MnS inclusion (such as the ones in Fig. 2e, f, h–k, n–q) or within MnS but close to the interface of MnS/steel matrix (Fig. 2a–d, g, l, m, r, s, v–x). That is to say, the interface which results from the presence of a particle within MnS medium provides an initial site where MnS dissolution occurs. The dissolutions of MnS around some of the particles seem to concentrically propagate into MnS matrix (Fig. 2a, m, s, x), while others like those in Fig. 2c, i, n–p, r, v behave in a different way.

Fig. 3 shows the size distributions of the nano-particles before and after the corrosion tests. They follow a similar spectrum according to statistical measurements on hundreds of particles, implying that the particles remain unchanged during catalysing MnS dissolution.

3.2. *Identification of the nano-particle catalysing MnS dissolution*

Various TEM techniques were applied to identify crystallographic characteristics of the nano-particles which catalyse MnS dissolution. The lattice type of these fine particles was determined on the basis of electron diffraction experiments. Sometimes the particles were so fine that we had to apply nano-beam to get electron diffraction patterns (EDPs) from a single grain. Fig. 4a is a bright-field TEM image in which two nano-particles embedded in MnS medium are arrowed. The darker contrast of the particles in this bright-field mode (rather than HAADF mode) indicates that they are parallel or close to a low-indexed zone axis. Fig. 4b–i shows a series of EDPs and their angular

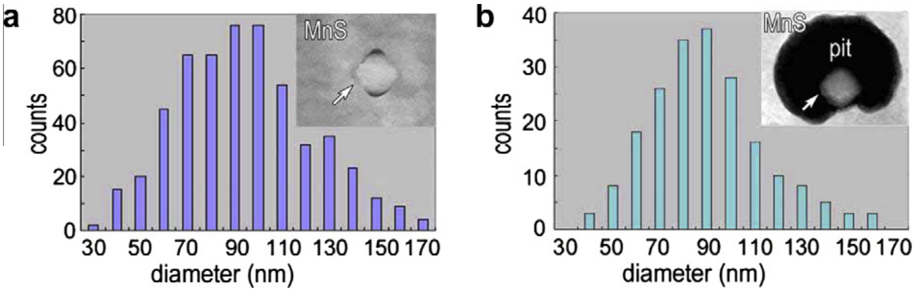

Fig. 3. (a) Size distributions of the particles before corrosion test obtained statistically from >500 particles. (b) Size distributions of the particles within pits after the corrosion test, derived from statistic measurements on >200 particles. It is seen that the size distribution follows similar spectrum, indicating that particle size has no change before and after MnS dissolution. The inset in each figure is a typical particle for statistical measurements.

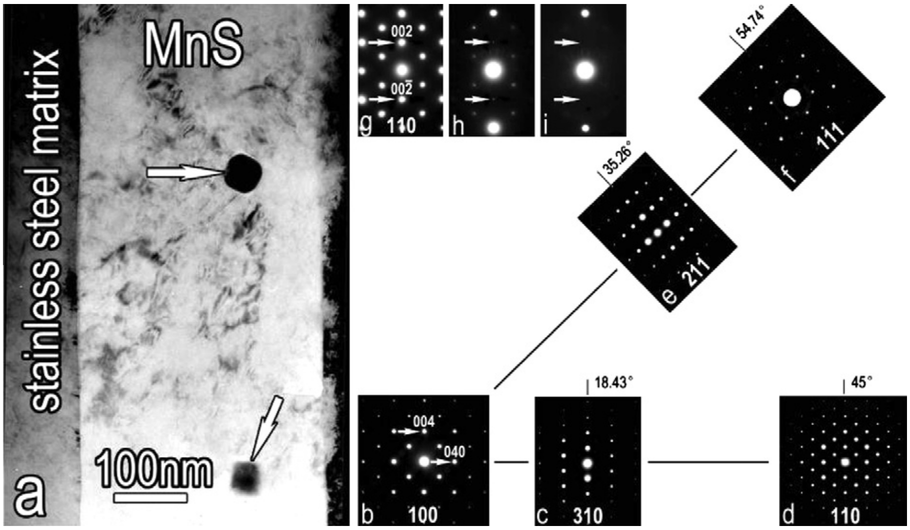

Fig. 4. Lattice-type determination of the nano-particle. (a) Bright-field TEM image in which two particles embedded in MnS medium are arrowed. (b–i) A series of EDPs obtained from the particles shown in (a) by large-angle tilting experiments. An fcc lattice is reconstructed according to the configuration of each pattern and the angular relationships between two patterns. The space group of $Fd\,\bar{3}m$ is derived based on the extinction rules in the EDPs.

relationships obtained from the particles shown in Fig. 4a by large-angle tilting experiments. A face-centered cubic (fcc) phase is determined according to the configuration of each pattern and the angles between two patterns. It is seen that the $(0\,k\,0)$ indices in [1 0 0] EDP are extinction when $k \neq 4n$ (here n is integral numbers). This is also the case for $(0\,0\,l)$ indices in [1 0 0] EDP. This implies that there is a d glide in (1 0 0) plane. In addition, the $(0\,0\,l)$ spots with $l = 2n$ in [1 1 0] EDP tend to vanish when we

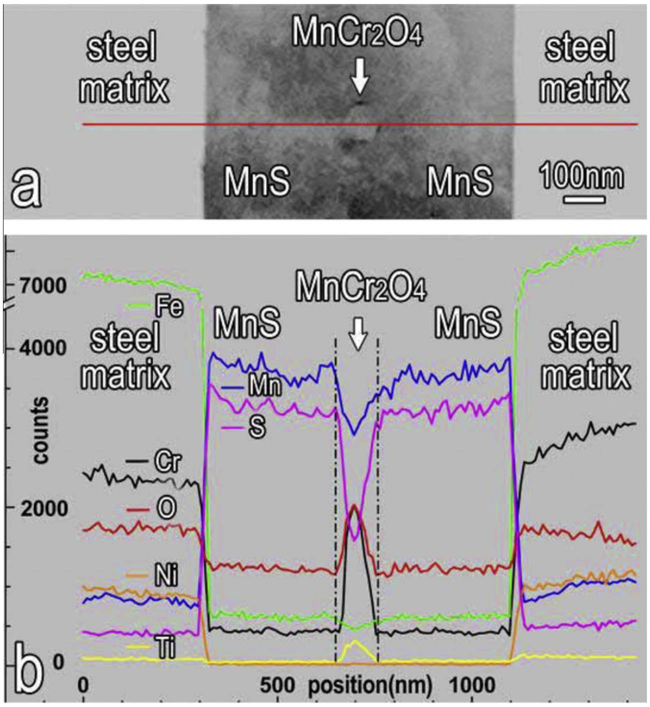

Fig. 5. Compositional analysis on a fine particle embedded in the MnS medium. (a) HAADF image showing a spatial distribution of steel matrix, MnS inclusion, and a small particle within MnS. (b) EDS profiles scanned along the red line marked in (a). The particle is composed mainly of Mn, Cr, and O, with a small amount of Ti. (For interpretation of the references to colour in this figure legend, the reader is referred to the web version of this article.)

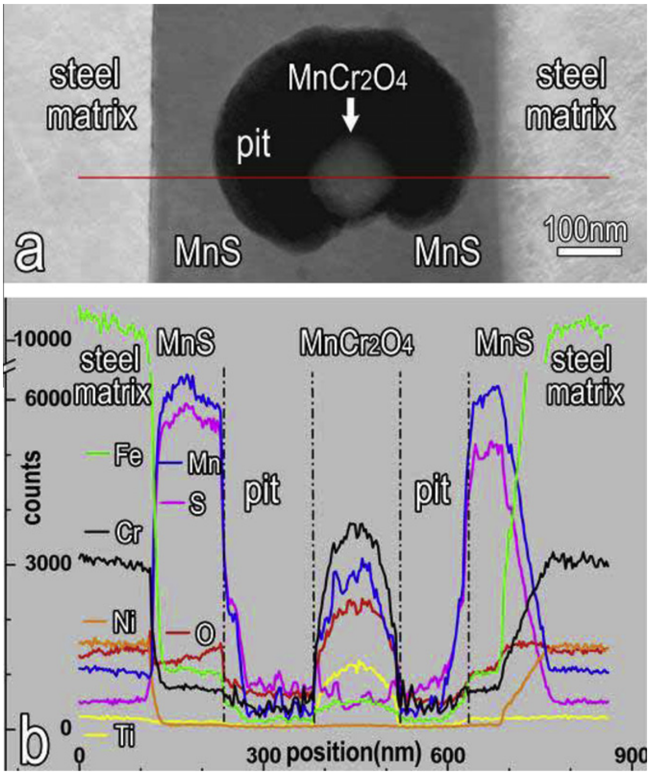

Fig. 6. Composition analysis on a nano-$MnCr_2O_4$, around which MnS dissolution occurs in the presence of salt water. (a) An HAADF image showing a pit in MnS around a particle. (b) The EDS results of a scan made along the red line in (a). The pit contributes little to MnS signals, which provide a clear imprint of MnS dissolution. (For interpretation of the references to colour in this figure legend, the reader is referred to the web version of this article.)

gradually tilted the crystal about the a^* axis (Fig. 4g–i), which indicates that these spots result from second diffractions. Therefore, the space group of $Fd\bar{3}m$ is derived based on these extinction rules. Such a structure is isotypic with diamond and other spinel phases (with formula of AB_2O_4), which belong to one of the major compound families in ceramics. The lattice parameter of this compound was determined to be $a = 0.84$ nm.

We then carried out detailed chemical composition analysis on these spinel-type particles. An example is shown in Fig. 5a, where a small particle marked with a downward arrow is embedded by the surrounding MnS medium in the HAADF image. The EDS profiles shown in Fig. 5b are obtained from the line-scanning along the red line in Fig. 5a. It is revealed that the particle is composed mainly of chromium, manganese, oxygen, and a very small amount of titanium. A combination of lattice parameter and chemical compositions concludes that such a compound corresponds to spinel $MnCr_2O_4$, or $Mn(Cr,Ti)_2O_4$ if small amount of titanium is taken into account. Composition analyses were also performed on the particles around which MnS was dissolved, as exampled in Fig. 6a. Fig. 6b shows the EDS results of a scan made along the red line in Fig. 6a, which reveal that the composition of the particle is the same as that before catalysing MnS dissolution. Generally speaking, before corrosion test the $MnCr_2O_4$ particles overlaps, more or less, with MnS medium (for example, Fig. 5b) or with both MnS and the steel matrix (for example, Fig. 2c). Such an overlapping may gradually decrease with the dissolution of MnS. As a consequence, the relative intensity of Mn signals before corrosion test is usually stronger than that after corrosion test. Electron diffraction experiments confirm that all the particles, around which MnS dissolution happened, have $MnCr_2O_4$-spinel structure with the same lattice parameter as that before MnS dissolution. In this spectrum of Fig. 6b, the steel matrix and MnS

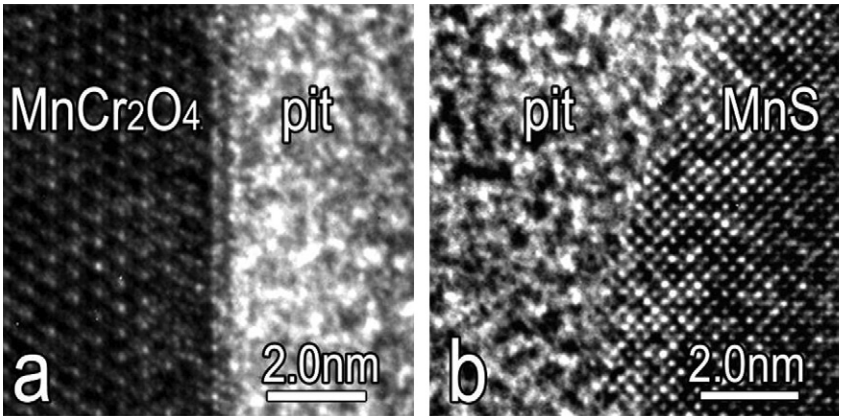

Fig. 7. (a) An HREM image at the pit/$MnCr_2O_4$ interface, taken along the [1 1 0] direction of $MnCr_2O_4$. (b) An HREM image at the MnS/pit interface, along $[1\ 0\ 0]_{MnS}$. The $MnCr_2O_4$/pit interface is sharp while that of MnS/pit is irregular, indicating that the $MnCr_2O_4$ particle is not involved in the dissolution of surrounding MnS.

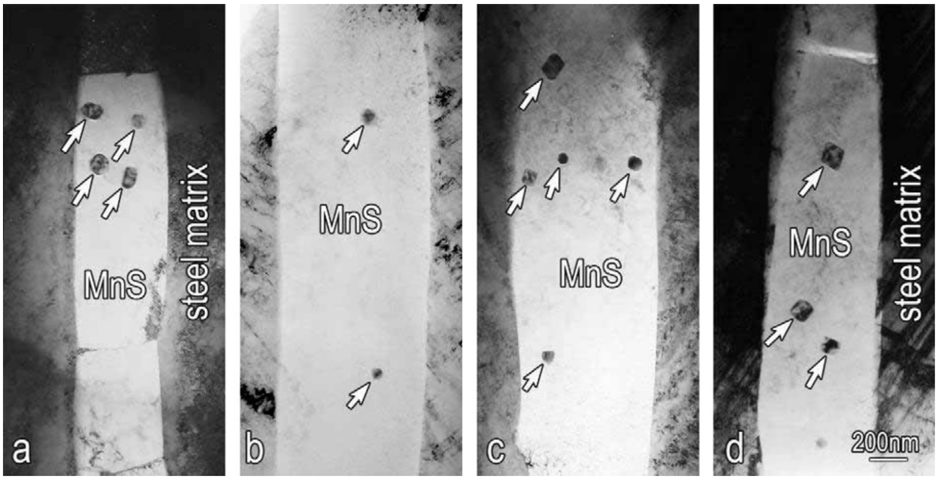

Fig. 8. Low-magnification bright-field TEM images showing a number of MnS sections in which nano-sized spinel $MnCr_2O_4$ particles (arrowed) are distributed in a scattered manner. The dark contrast in the bright-field TEM mode means that these particles lie in or are close to a zone axis direction. These $MnCr_2O_4$ particles usually have specific geometric morphologies. Note that these images are at the same magnification.

inclusion are well identified. Signals of very little amplitude are detected around the central particle, which supplies a clear proof of a pit due to MnS dissolution.

High-resolution TEM imaging shows that the remains of the MnS dissolution are structurally disordered. Fig. 7a is an HREM image, obtained along the [1 1 0] direction of $MnCr_2O_4$, showing the interface between $MnCr_2O_4$ and the pit. Fig. 7b is an HREM image taken at MnS/pit along the $[1\,0\,0]_{MnS}$ direction. It is seen that the interface of $MnCr_2O_4$/pit is sharp while that of MnS/pit is irregular, confirming that the $MnCr_2O_4$ nano-particle had changed little while MnS dissolved.

Removing coarse-size oxide inclusions (usually at micrometer scale) has been one of the major concerns in steelmaking processing, since it is known that they are not deformable and are consequently harmful to the mechanical properties of steels [30,31]. With the development of modern refining process, manufacturers are now able to

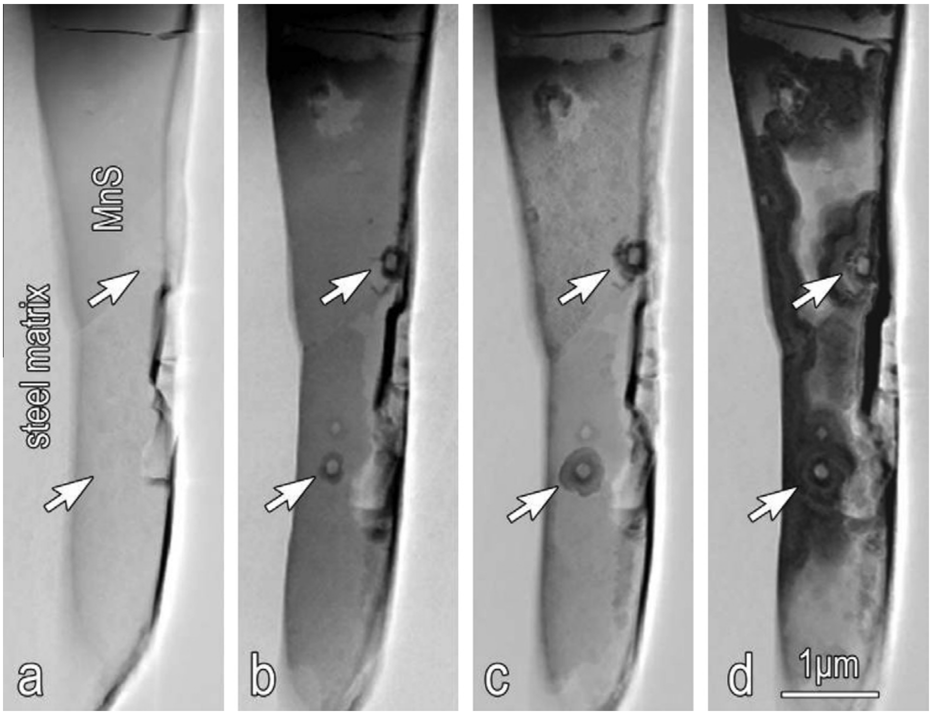

Fig. 9. In situ ex-environmental TEM showing a continuous development of a pit vs. immersion duration in a fixed MnS inclusion where two $MnCr_2O_4$ particles are marked with arrows. The formation of pit results from the dissolution of MnS around the $MnCr_2O_4$ particle. The micrographs are recorded in the HAADF mode. (a) Before immersion, the contrast difference between $MnCr_2O_4$ particles and the MnS medium is small, which is due to the similar high-angle scattering of the elements in these two compounds. (b) After 15 min immersion in 1 M NaCl solution. (c) After 30 min immersion. (d) After 60 min immersion. It is seen that the pits around the $MnCr_2O_4$ particles spread with the increasing of immersion duration.

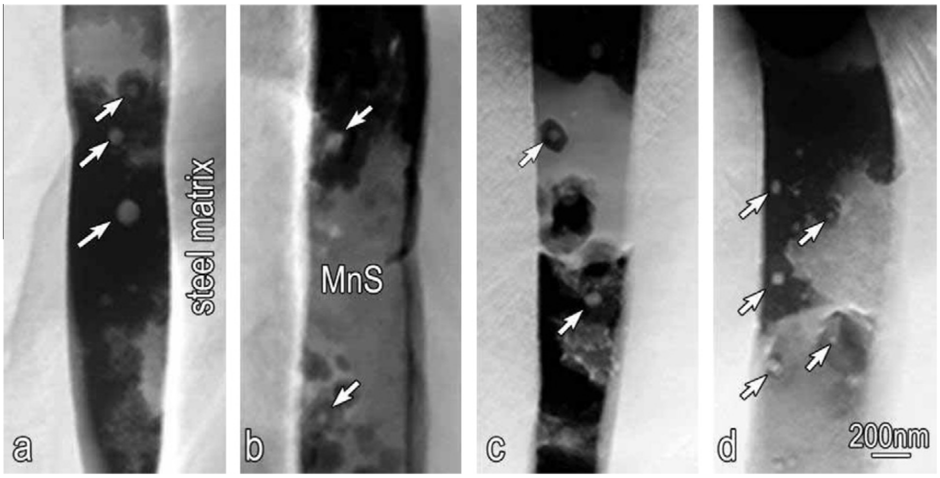

Fig. 10. HAADF images showing several MnS inclusion sections which suffered from serious dissolution after the specimens experienced over 90 min corrosion. It is seen that in each MnS inclusion a large area is involved in the dissolution. Some of the $MnCr_2O_4$ particles in the pits are arrowed.

largely reduce the dimensions of the unexpected oxides to meet the demand for high-purity steels [32]. Nevertheless, it is easy for oxide inclusions to be present, and they are known to nucleate in the first stage of solidification

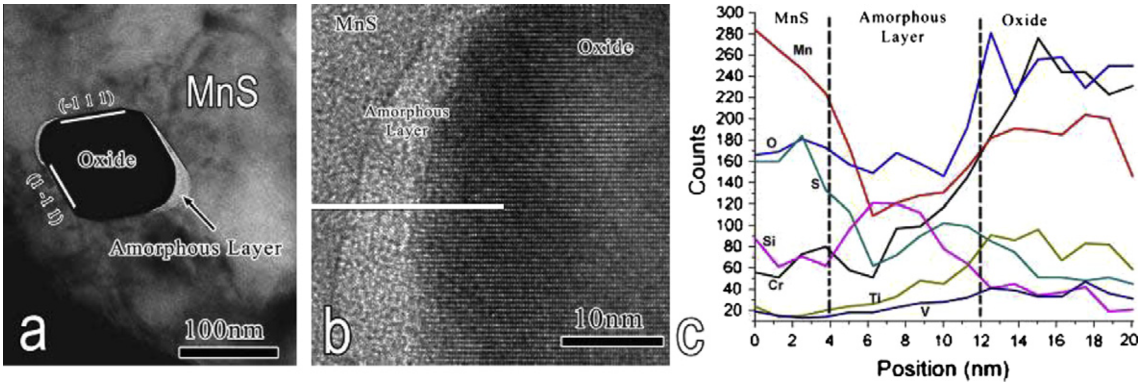

Fig. 11. Microstructural characteristics at the interface of $MnCr_2O_4$/MnS. (a) A typical bright-field TEM image of an $MnCr_2O_4$ crystal and the $MnCr_2O_4$/MnS interface. Note that there are two arc-shaped regimes perpendicular to the rolling direction, which are believed to be induced by the deformation mismatch between $MnCr_2O_4$ and MnS. (b) An HREM image indicating that the arc-shaped regimes in (a) are structurally disordered. (c) EDS analysis showing a segregation of silicon and oxygen in this local regime. Nevertheless, a series of corrosion tests concludes that such an amorphous-like regime does not make MnS preferentially dissolved.

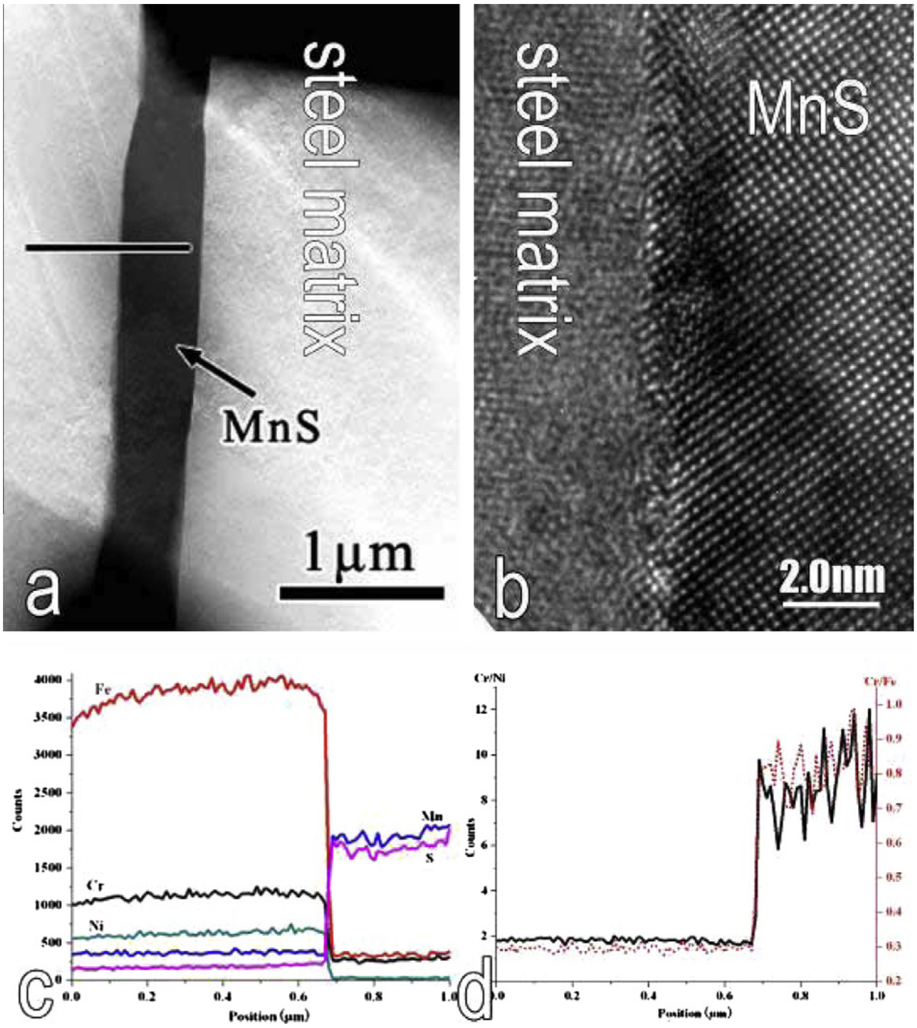

Fig. 12. Interface characteristics of MnS/steel matrix. (a) An HAADF image of MnS inclusion (arrowed) together with steel matrix. (b) An HREM image showing that the interface is sharp, which implies that there is no intermediate zone between two phases. (c) EDS results of a scan made along the line in (a), traversing the steel matrix into MnS inclusion. (d) Relative composition profiles of Cr derived by Cr/Ni and Cr/Fe according to the data in (c).

[33–35]. In the casting process, oxygen may precipitate due to its relatively lower solubility in solid austenite compared with that in the molten state. This results in the formation of MnO and Cr_2O_3 first and then of spinel $MnCr_2O_4$ crystals when the steel is annealed or hot-rolled. The spinel $MnCr_2O_4$ particles identified in this study, although they are in the nanometer scale, are present in almost all the MnS inclusions. These nano-$MnCr_2O_4$ particles have random orientations, and are located either in the inner part of MnS inclusion or within MnS but close to the interface of the MnS/steel matrix (see also Fig. 2). Fig. 8 shows several MnS sections where we can see that the nano-$MnCr_2O_4$ particles in each section are dispersedly distributed. In addition, the nano-particles feature specific lineament, which implies that they own particular geometric morphology in three dimensions. The presence of such ultra-fine inclusions has received little attention, particularly in engineering.

3.3. In situ development of MnS dissolution vs. duration of immersion in salt water

The in situ TEM observation provides more details on crystallography and morphology for understanding the electrochemical processes. In the present study, the duration of immersion in 1 M NaCl solution for corrosion test ranged from 5 to 90 min. An invariable phenomenon in all these experiments is that the local dissolution of MnS occurs initially at the interface of MnS/$MnCr_2O_4$: where there is an $MnCr_2O_4$ particle, MnS dissolution occurs. We find that MnS inclusions have no remarkable changes when the immersion is less than 10 min at room temperature. In contrast, most MnS inclusions are seriously dissolved after immersion for 60 min. In situ observation also shows that, once the dissolution of MnS occurs, it develops with the duration of immersion in the salt water. Fig. 9a–d shows HAADF images illustrating a continuous development of the pits vs. immersion duration from 15 min up to 60 min. Fig. 9a is an image before corrosion test. It can be seen that $MnCr_2O_4$ particles and the surrounding MnS share similar contrast, which results from the fact that these two compounds share similar mass characteristics. However, the presence of the $MnCr_2O_4$ particles and their dimensions are clearly seen after MnS is dissolved. It can be seen from Fig. 9b–d that the pits around the $MnCr_2O_4$ particles (marked with arrows) gradually spread with increasing immersion duration. During the whole stage of MnS dissolution, the dimensions of the $MnCr_2O_4$ particles remain unchanged.

Fig. 10a–d shows HAADF images with several MnS sections experiencing a corrosion test of over 90 min. The dissolution of MnS around some of the $MnCr_2O_4$ particles

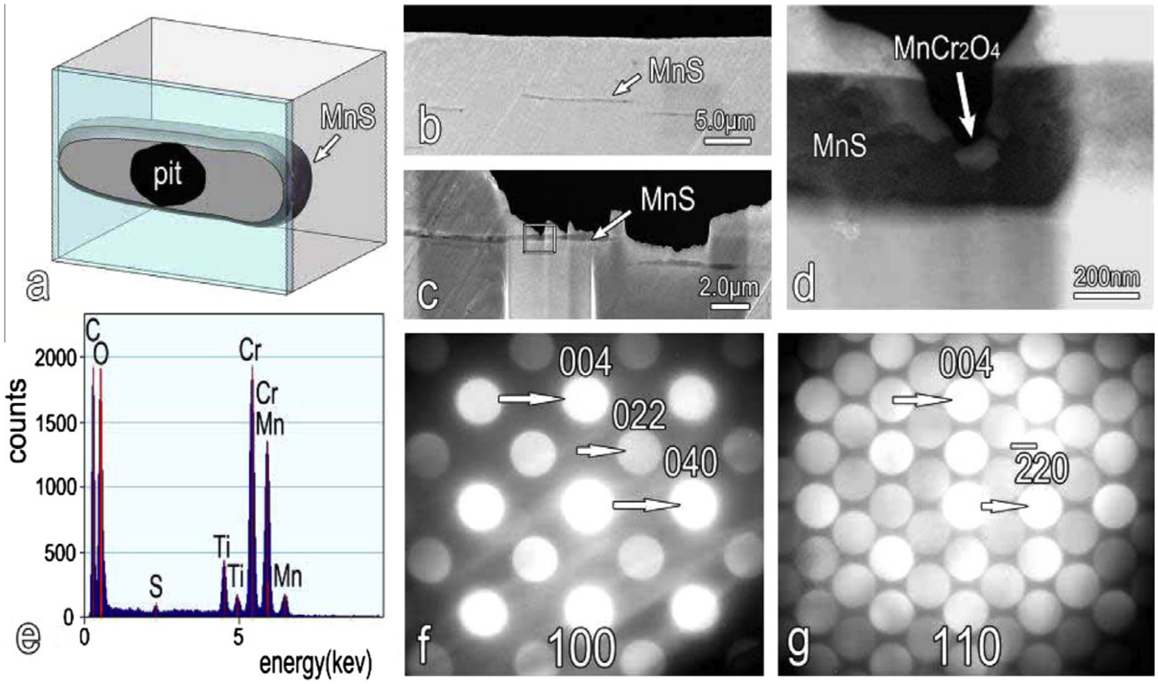

Fig. 13. Corrosion test in bulk sample. (a) Schematic illustration of TEM specimen preparation by using an FIB from a bulk sample experienced corrosion. The area to be cut was selected on the basis of the fact that a target MnS inclusion slightly dissolved. The principle of the cutting was to remove the back side of the corroded surface and obtain an electron-transparent TEM specimen (the blue thin piece). (b) SEM image of the sample after corrosion in which an MnS inclusion (arrowed) slightly dissolved and was chosen for FIB cutting. (c) SEM image of the target MnS inclusion cut by FIB. The outlined area was originally corroded. (d) Zoom-in image of the central area suffered the corrosion, where a fine particle is observed. (e) EDS analysis of the particle showing the components of Cr, Mn, O, and a small amount of Ti. The carbon peak is believed to result from the specimen contamination. (f) and (g) are EDPs of $MnCr_2O_4$ with [1 0 0] and [1 1 0] zone axis, respectively. (For interpretation of the references to colour in this figure legend, the reader is referred to the web version of this article.)

was so great that the pits grew and coalesced. In such a case, the dissolution develops across the MnS inclusion and spreads to the interface of the MnS/steel matrix. It is known that stainless steel resists corrosion because of the formation of a passive film of chromium oxide. According to the present study, it is proposed that a complete dissolution of MnS may directly expose steel matrix, which was originally underneath MnS inclusion, to the wet environment. The resultant steel matrix without coverage of passive film may suffer further corrosion in the presence of salt water. Another remarkable feature in the present experiments is that a fixed MnS has variant degree of local dissolution around different $MnCr_2O_4$ particles with similar dimensions, as seen in Figs. 1 and 10. This phenomenon implies that the $MnCr_2O_4$ particles have different surface reactivity in catalysing MnS dissolution.

In this study particular attention has been paid to the microstructural characteristics at the interface of $MnCr_2O_4$/MnS. Fig. 11a is a typical bright-field TEM image of an $MnCr_2O_4$ crystal and the $MnCr_2O_4$/MnS interface where we can see arc-shaped regimes perpendicular to the rolling direction. The $MnCr_2O_4$ particle, which has a specific geometric morphology, is proposed to be un-deformed while MnS was elongated in the hot-rolling process. The arc-shaped regimes at the MnS/$MnCr_2O_4$ interface are believed to be induced by the deformation mismatch between $MnCr_2O_4$ and MnS. Such a case may happen to a multi-phase system in which a harder particle is embedded in a softer matrix. The HREM image shown in Fig. 11b indicates that the arc-shaped regimes in Fig. 11a are structurally disordered. EDS analysis as that in Fig. 11c shows a segregation of silicon and oxygen in this local regime. In the HAADF mode, such an amorphous-like regime is in darker contrast, as seen in Fig. 1d, since it is rich of light elements. However, a series of corrosion tests conclude that the amorphous-like regime does not make MnS preferentially dissolved. In addition, local deteriorations in MnS, such as cracks or voids resulting from materials processing (the central area of MnS in Fig. 1b and c), have a negligible influence on MnS dissolution. In other words, it is the nano-sized oxide embedded in MnS, rather than other deteriorations, that catalyses the local dissolution of MnS.

Pitting corrosion is the localized dissolution of an oxide-covered metal in specific aggressive environments, and is one of the common and catastrophic causes of the material's failure. Although prediction of the time and location of pitting events is extremely difficult, an undisputed aspect

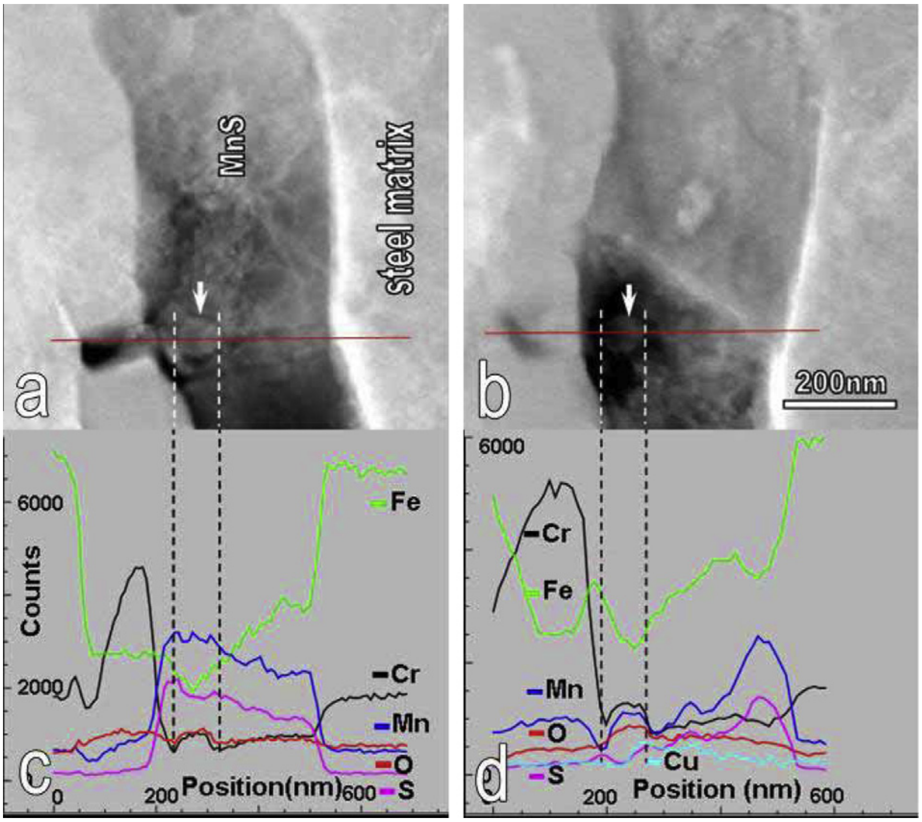

Fig. 14. In situ ex-environment experiment carried out in 304-type stainless steel. (a) An HAADF image of an MnS section in which a fine particle is embedded (arrowed). (b) The same section as in (a) but having experienced 75 min immersion in salt water. Note that the MnS is locally dissolved and this occurs around a particle. (c) EDS results of a scan made along the red line in (a). (d) EDS results of scan, after the corrosion test, along the red line in (b), which is the same path as that in (a). The composition of the particle before and after MnS dissolution remains unchanged. This particle is spinel $MnCr_2O_4$ as well, the same as that in 316F steel. (For interpretation of the references to colour in this figure legend, the reader is referred to the web version of this article.)

is that pitting corrosion of stainless steel is strongly associated with the local dissolution in MnS inclusion on the basis that the majority of pitting events are found to occur at, or adjacent to, MnS inclusion [6,7]. Nevertheless, the initial location where MnS dissolution preferentially occurs was unknown. By means of secondary ion mass spectroscopy (SIMS) analysis, Ryan et al. described the presence of a wide Cr-depleted zone around MnS inclusions in a stainless steel, and suggested that pitting could be triggered by an attack on these Cr-depleted zones instead of at the MnS inclusions themselves [19]. In contrast, Meng et al. found no evidence of Cr-depleted zones in a number of stainless steels using high-resolution scanning transmission electron microscopy and SIMS mapping [20,36]. In the beginning of our present study, we also focused on the nano-scaled composition analysis at the interface of MnS/steel matrix. Fig. 12a is an HAADF image of MnS inclusion (arrowed) together with steel matrix. Fig. 12b is an HREM image showing the interface details, taken along $[0\ 1\ 0]_{MnS}$. The 2D lattice fringe of the steel matrix cannot be imaged in this direction, since MnS and the surrounding matrix have no fixed orientation relationships. It is seen in Fig. 12b that the interface is sharp, which implies that there is no intermediate zone between two phases. Fig. 12c shows the EDS results of a scan made along the line in Fig. 12a, traversing the steel matrix into MnS inclusion. The composition profiles are sharply switched from phase to phase. Fig. 12d shows relative composition profiles of Cr derived by Cr/Ni and Cr/Fe according to the data in Fig. 12c. Cr-depleted zone is not found

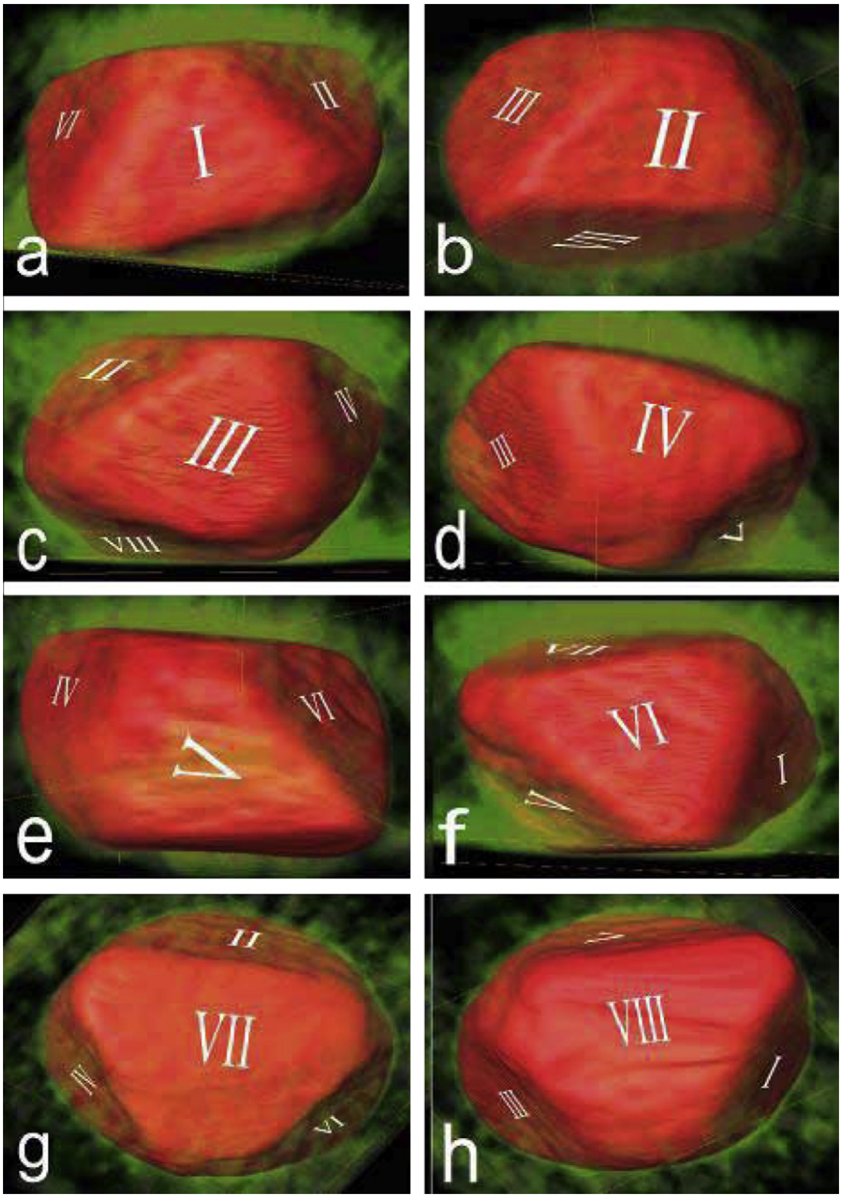

Fig. 15. Identification of an octahedron by means of large-angle tilting experiments and 3D tomography. The octahedron is enclosed by eight triangles labelled with I, II, III... VIII, respectively.

around the MnS inclusion; instead we uncovered the presence of nano-sized oxides embedded in MnS medium and clarified their catalysing role in MnS dissolution by means of in situ ex-environmental TEM (Figs. 1, 2, 9 and 10).

In order to exclude any effect of thin-foil TEM specimen on the corrosion mechanism, corrosion tests were also performed on bulk samples in 1 M NaCl solution for 60 min. After selecting a target MnS inclusion under SEM which slightly dissolved, we prepared a cross-sectional TEM specimen of the corroded area by using the FIB technique, as schematically shown in Fig. 13a. Such a corroded area was closely monitored during the FIB cutting (Fig. 13b and c). Bright-field TEM imaging identified the presence of a fine particle at the central area (pit) of MnS dissolution (Fig. 13d). EDS (Fig. 13e) and EDPs (Fig. 13f and g) analyses clarified it to be spinel $MnCr_2O_4$. This finding confirms the fact that it is the nano-$MnCr_2O_4$ that catalyses the local dissolution of MnS in 316F stainless steel.

To further confirm the universality of this phenomenon, other commercial stainless steels, such as 304-type, with relatively lower sulphur content, has been investigated as well. Fig. 14a is an HAADF image of an MnS section in the 304 steel, and Fig. 14b is the same section but after having been immersed for 75 min in salt water. It is seen in Fig. 14b that the MnS is locally dissolved and this occurs around a particle, which is the same as that frequently observed in 316F stainless steel (Figs. 1 and 2). Fig. 14c shows the EDS results of a scan made along the red line in Fig. 14a, traversing the steel matrix into oxide/MnS inclusion and back to the steel matrix. Fig. 14d shows the EDS results of scan, after the corrosion test, along the red line in Fig. 14b, which is the same path as that in Fig. 14a. A comparison of EDS profiles in Fig. 14c and d indicates that the composition of the particle, around which the local dissolution of MnS occurred, is the same before and after corrosion test. It is composed mainly of Mn, Cr, and O. The EDS profiles combined with electron diffraction analysis (not shown here) confirm that in 304-type steel there are also nano-$MnCr_2O_4$ particles embedded in the MnS medium and these particles result in the local dissolution of MnS inclusion.

3.4. Determination of $MnCr_2O_4$ nano-octahedron and its reactivity

Based on a series of experiments shown in the above sections, it is concluded that the inhomogeneous dissolution of MnS is strongly associated with the presence of endogenous nano-oxides embedded in the MnS medium (Figs. 1 and 2). However, not all the $MnCr_2O_4$ particles are reactive in catalysing the dissolution, which implies that these nano-particles have different reactive surfaces. By means

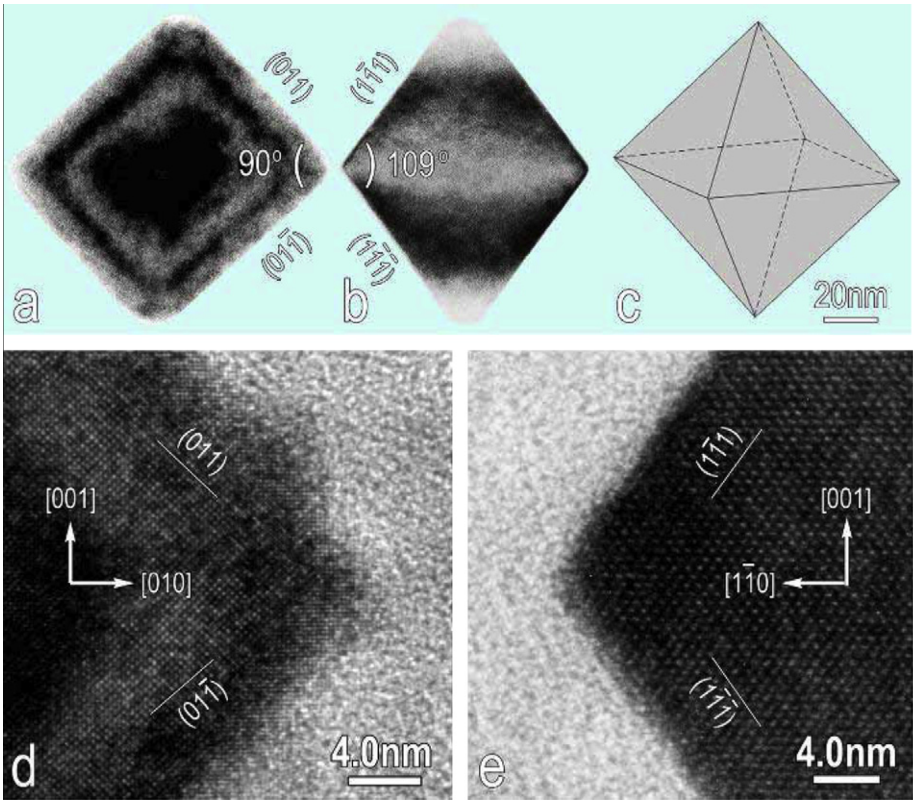

Fig. 16. Geometric identification of $MnCr_2O_4$ nano-octahedron by conventional TEM techniques. (a) A bright-field TEM micrograph of an $MnCr_2O_4$ octahedron imaged along the [1 0 0] direction. (b) TEM micrograph of the same $MnCr_2O_4$ octahedron as that in (a) but imaged along the [1 1 0] direction. (c) Schematic illustration of an ideal octahedron. (d) HREM images of an octahedron taken along the [1 0 0] direction. (e) HREM images of an octahedron taken along the [1 1 0] direction. The amorphous-like area around $MnCr_2O_4$ octahedron results from the dissolution of MnS.

of large-angle tilting experiments and 3D tomography in the TEM, we found that these nano-particles have specific geometric shape, which was identified to be an octahedron enclosed by eight triangles. The 3D morphology of an octahedron is displayed in Fig. 15, where each of the {1 1 1} planes is alternately shown up.

The geometry of the $MnCr_2O_4$ nano-octahedron can also be derived based on conventional TEM images taken along various low-indexed directions. Fig. 16a is a bright-field TEM micrograph of an $MnCr_2O_4$ particle imaged along the [1 0 0] direction, and Fig. 16b is a micrograph of the same particle as that in Fig. 16a but imaged along the [1 1 0] direction. The angular relationships between different planes (marked in the figures) almost follow the parameters of an ideal octahedron, as schematically illustrated in Fig. 16c. Fig. 16d and e shows HREM images of the octahedron taken in the areas corresponding to the corners in Fig. 16a and b. The lattice images in the HREM micrographs agree well with the indexing in Fig. 16a and b. The amorphous-like regime around the $MnCr_2O_4$ octahedron results from the dissolution of MnS.Spinel-type structure is one of the major families in ceramics. Fig. 17a is the atomic configurations in one unit cell of $MnCr_2O_4$. Fig. 17b is the atomic projection along the [1 1 0] direction, where (1 1 1) planes are stacked along the $[\bar{1}\,1\,1]$ direction. It is seen that a (1 1 1) plane of the fcc $MnCr_2O_4$ has four

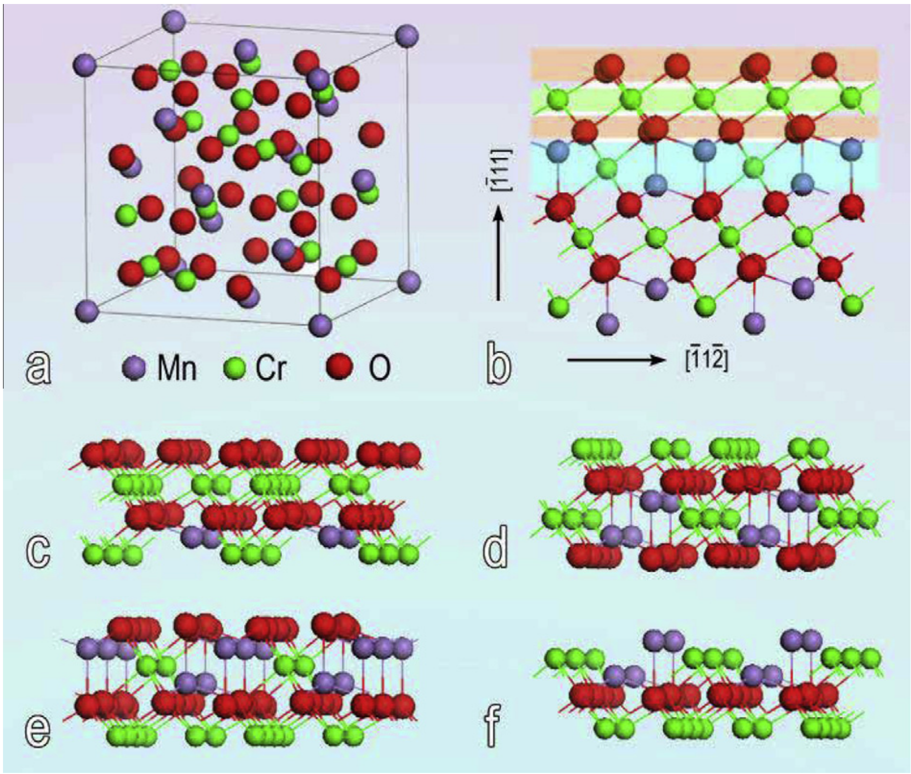

Fig. 17. Crystal structure of spinel $MnCr_2O_4$. (a) 3D atomic configuration in a unit cell of spinel $MnCr_2O_4$. (b) Atomic projection of the structure along the [1 1 0] direction. Four (1 1 1) sub-layers are highlighted. (c) Atomic configurations where oxygen ions are located at the (1 1 1) surface layer, and Cr ions are underneath oxygen (this is designated as O–Cr configuration). (d) Atomic configurations where Cr ions are located at the terminal layer (Cr–O configuration). (e) Atomic configurations where O–Mn puckered layer is at the terminal (O–Mn configuration). (f) Atomic configurations where Mn–Cr puckered layer is at the terminal.

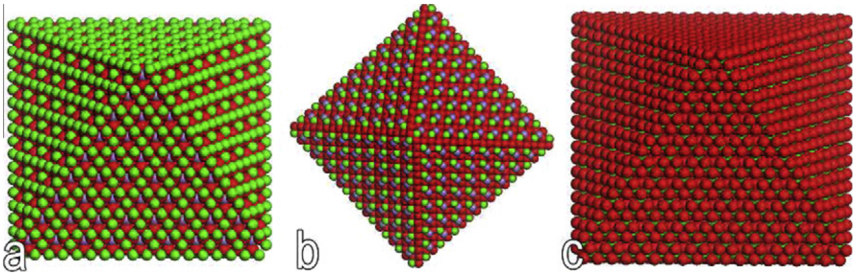

Fig. 18. Structure models of an octahedron with variant terminal layers. (a) Cr-terminated octahedron. (b) Mn-terminated octahedron. (c) O-terminated octahedron. The reactivity of an octahedron strongly depends on the terminal ions at the surface.

sub-layers: two O-terminated layers and two metal-terminated ones (highlighted). Based on such a layered stacking, variant 3D structures with different surface configurations are displayed in Fig. 17c–f. If an octahedron is enclosed with metal species, such as that schematically shown in Fig. 18a and b, it is termed a metal-terminal octahedron. In contrast, if enclosed with oxygen, it is an O-terminal octahedron (Fig. 18c).

It is known that corrosion can be considered as a catalytic process in the presence of a microgalvanic cell. In the present system of $MnS/MnCr_2O_4$, MnS dissolution is catalysed by the nano-$MnCr_2O_4$, which can be rationalized at an atomic level as follows. On the anode (MnS), MnS dissolution occurs, while the oxygen reduction reaction (ORR) takes place on the cathode ($MnCr_2O_4$):

$$O_2 + * \rightarrow O_2(ad) \tag{1}$$

$$O_2(ad) + * \rightarrow 2O(ad) \tag{2}$$

$$H_2O + * \rightarrow H_2O(ad) \tag{3}$$

$$O(ad) + H_2O(ad) \rightarrow 2OH(ad) \tag{4}$$

where $*$ denotes an active site on the surface, and ad is the abbreviation of adsorption. The rates of the two reactions should be equal at any time since there is no bias applied to this system. So, we can assess the rate of MnS dissolution reaction by evaluating the rate of ORR. DFT calculations were applied to each of the four surfaces. For adsorption sites, all the possible sites were considered and the most stable adsorption site was marked in the energy profiles mentioned below. Fig. 19 shows plan views and side elevations of O_2 adsorption structures on the four $MnCr_2O_4$ {1 1 1}

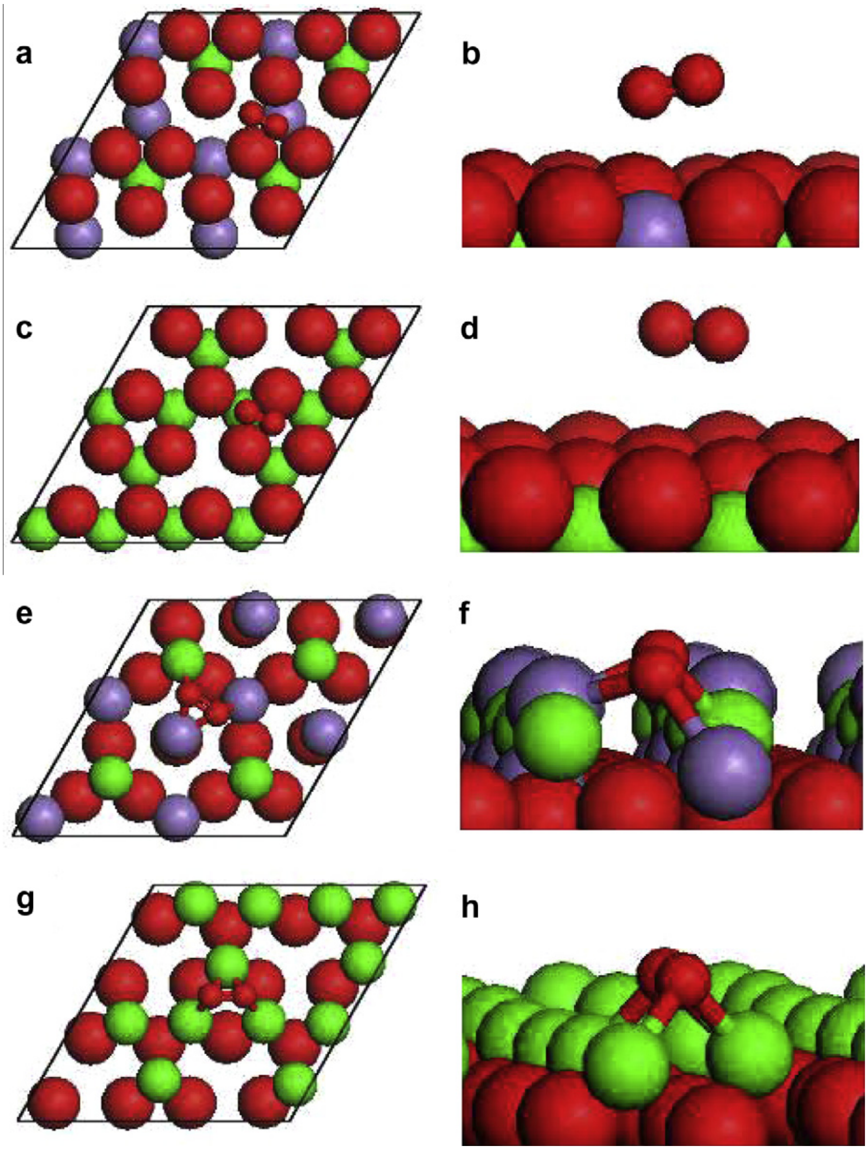

Fig. 19. Plan views and side elevations of O_2 adsorption structures on the four $MnCr_2O_4$ (1 1 1) surfaces. (a) and (b), (c) and (d), (e) and (f), (g) and (h) represent O–Mn, O–Cr, Mn–Cr, Cr–O surfaces, respectively. The O–O bond lengths in the four adsorption structures are 1.236 Å, 1.236 Å, 1.541 Å, 1.494 Å, respectively, and the vertical distances of O_2 and surface atoms are 2.458 Å, 2.854 Å, 0.514 Å, 1.323 Å, respectively.

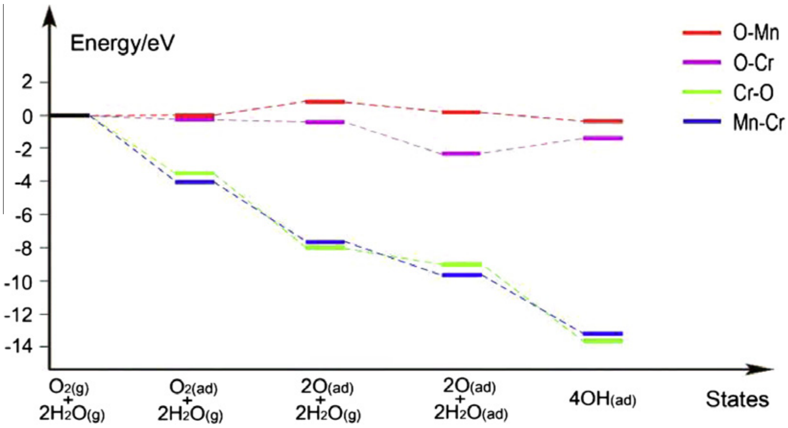

Fig. 20. Energy profiles of the ORR on four different (1 1 1) surface atomic configurations. For each surface, there are five solid bars, indicating five different adsorption states and four dashed lines, indicating four reactions as mentioned in the text. The energy differences of these states are the reaction enthalpies. It is seen that the reaction happens easily on the surface with metal terminations.

surfaces. The energy profiles of the ORR reaction pathways on the four surfaces are plotted in Fig. 20, and these indicate that the atomic configurations on the surface of the octahedron play a critical role in the rate of ORR. Two striking features are revealed from the calculations. Firstly, two metal-terminated surfaces are much more energetically favoured for ORR than O-terminated ones. Secondly, it is found that O_2 adsorption, which is a key step in the ORR, cannot occur on any O-terminated surfaces; optimized geometries show that O_2 is far away from the O-terminated surfaces and the O–O distance is identical to the gas phase one, indicating that the interaction between O_2 and O-terminated surfaces is very weak. This is consistent with the energy profile (the two top curves in Fig. 20), which shows that no adsorption energy gain is obtained in O_2 adsorption. In contrast, optimized geometric structures of O_2 adsorption on the metal-terminated surfaces reveal that adsorbed O_2 is highly activated by the surfaces with long O–O distances (over 20% longer than that in the gas phase), which is in accordance with the large chemisorption energies illustrated in Fig. 20. Therefore, the $MnCr_2O_4$ nano-octahedron with metal terminations is more reactive in catalysing the MnS dissolution than O-terminated ones.

Although the present nano-oxide (spinel) particles are basically octahedral, the terminal surfaces are more or less puckered (Fig. 15). In such a case, non-{1 1 1}-planes with small area are locally present at the surface of the octahedron. In addition, a single active octahedron may be composed of metal- and also local oxygen-terminal surface. An octahedron with larger area of metal terminations is more reactive than that with few metals. This should be the reason we found various MnS dissolution behaviors around different $MnCr_2O_4$ particles (Fig. 2).

Because of scientific and technological importance, inorganic single crystals (such as anatase TiO_2 and spinel Co_3O_4) with highly reactive surfaces have long been studied particularly in catalyst and energy/environmental fields [37–40]. In the case of free-standing nano-particles, surfaces with high reactivity usually diminish rapidly during the crystal growth as a result of the minimization of surface energy. In contrast, the single-crystallized $MnCr_2O_4$ nano-octahedra identified in this study are endogenous and embedded in the steel, so these octahedra may differ from each other by different atomic configurations on their surface. This should be the reason why we find that some octahedra are active and some are inactive, namely, the dynamics of MnS dissolution is the function of the species of terminal ions enclosing the nano-octahedron catalyst.

So far, little attention has been paid to the ultra-fine inclusions in stainless steels, since they are understood not to undermine the mechanical properties of the steels. However, the nano-sized oxide particles identified in the present study are found to play a critical chemical role in catalysing MnS dissolution and pitting corrosion of the steels. The present findings are of great importance for the steel-making industry by calling for attention to be paid to nano-inclusions, the presence of which is normally neglected. This work is expected to draw the attention of material scientists, chemists, and biomedical workers to a general concern that the phenomena similar to those in this study may occur in a wide range of engineering alloys and biomedical materials/instruments serving in wet environments.

4. Conclusions

We have applied in situ ex-environment transmission electron microscopy to identify the initial site, at an atomic scale, of MnS dissolution, which is critically important but unclear so far for understanding the origin of pitting corrosion in stainless steels. We find that a “single-grained” MnS inclusion in the steel is compositionally and structurally inhomogeneous. Fine octahedral precipitates of spinel $MnCr_2O_4$, with dimensions of several tens of nanometers, are dispersedly distributed in the MnS inclusions, generating local $MnCr_2O_4$/MnS nano-galvanic cells. In situ TEM studies indicate that the MnS initially dissolves at the $MnCr_2O_4$/MnS interface in the presence of salt water, and the dissolution gradually spreads outwards, leaving a pit around the $MnCr_2O_4$ octahedron. However, the reactivity of these octahedra is various. First-principles calculations indicate that the dynamics of MnS dissolution is the function of the species of terminal ions enclosing the nano-octahedron catalyst. The $MnCr_2O_4$ nano-octahedron with metal terminations is more reactive in catalysing the MnS dissolution than O-terminated ones. This work uncovers the origin of MnS dissolution in stainless steels and provides a new basis for understanding pitting corrosion of stainless steels.

Acknowledgements

We thank Profs. K. Lu and R. Yang for their full support and critical comments throughout this subject, which covers experiment design, selecting display items, and manuscript writing. We appreciate Mr B. Wu of this lab and Dr. E. Sourty of FEI (Shanghai) for the help with 3D tomography, and Dr. J. Tan for FIB sampling. X.L. Ma is also grateful to Profs. W. Ke and F.H. Wang at this institute, Prof. J.H. Park at University of Ulsan, S. Korea, Prof. D. Embury at McMaster University, Canada, and Prof. U. Köster at Dortmund University, Germany, for fruitful discussions. This work is supported by the National Natural Science Foundation of China and National Basic Research Program of China (2009CB623705). B. Zhang acknowledges the support from the Knowledge Innovation Program of the Chinese Academy of Sciences. P. Hu is supported by the CAS/SAFEA International Partnership Program for Creative Research Teams.

References

[1] Lyon S. Nature 2004;427:406.
[2] Punckt C et al. Science 2004;305:1133.
[3] Williams DE, Newman RC, Song Q, Kelly RG. Nature 1991;350:216.
[4] Jones RL. Mater Perform 1996;35:63.
[5] Collins JA, Monack ML. Mater Protect Perform 1973;12:11.
[6] Eklund GS. J Electrochem Soc 1974;121:467.
[7] Wranglen G. Corros Sci 1974;14:331.
[8] Castle JE, Ke R. Corros Sci 1990;30:409.
[9] Stewart J, Williams DE. Corros Sci 1992;33:457.
[10] Baker MA, Castle JE. Corros Sci 1993;34:667.
[11] Williams DE, Mohiuddin TF, Zhu YY. J Electrochem Soc 1998;145:2664.
[12] Frankel GS. J Electrochem Soc 1998;145:2186.
[13] Suter T, Webb EG, Böhni H, Alkire RC. J Electrochem Soc 2001;148:B174.
[14] Webb EG, Alkire RC. J Electrochem Soc 2002;149:B272.
[15] Muto I, Izumiyama Y, Hara N. J Electrochem Soc 2007;154:C439.
[16] Schmuki P, Hildebrand H, Friedrich A, Virtanen S. Corros Sci 2005;47:1239.
[17] Krawiec H, Vignal V, Heintz O, Oltra R. Electrochim Acta 2006;51:3235.
[18] Williams DE, Zhu YY. J Electrochem Soc 2000;147:1763.
[19] Ryan MP, Williams DE, Chater RJ, Hutton BM, McPhail DS. Nature 2002;415:770.
[20] Meng Q, Frankel GS, Colijn HO, Goss SH. Nature 2003;424:389.
[21] Williams DE, Westcott C, Fleischmann M. J Electrochem Soc 1985;132:1796.
[22] Newman RC. Nature 2002;415:743.
[23] Kresse G, Furthmuller J. Phys Rev B 1996;54(16):11169.
[24] Kresse G, Hafner J. Phys Rev B 1993;47(1):558.
[25] Perdew JP, Burke K, Ernzerhof M. Phys Rev Lett 1996;77(18):3865.
[26] Blochl PE. Phys Rev B 1994;50(24):17953.
[27] Wang L, Maxisch T, Ceder G. Phys Rev B 2006;73(19):195107.
[28] Hastings JM, Corliss LM. Phys Rev 1962;126(2):556.
[29] Pennycook SJ. Adv Imag Electron Phys 2002;123:173.
[30] Osio AS, Liu S, Olson DL. Mater Sci Eng A 1996;221:122.
[31] Park JH. Metall Mater Trans 2007;38B:657.
[32] Naito KI, Wakoh M. Scand J Metall 2005;34:326.
[33] Oikawa K, Sumi SI, Ishida K. J Phase Equilibr 1999;20:215.
[34] Wakoh M, Sawai T, Mizoguchi S. ISIJ Int 1996;36:1014.
[35] Tanahashi M et al. ISIJ Int 2003;43:7.
[36] Meng Q, Frankel GS, Colijn HO, Goss SH. Corros Sci 2004;60:346.
[37] Yang HG et al. Nature 2008;453:638.
[38] Jansson J et al. J Catal 2002;211:387.
[39] Petitto SC, Marsh EM, Carson GA, Langell MA. J Mol Catal A: Chem 2008;281:49.
[40] Xie XW, Li Y, Liu ZQ, Haruta M, Shen WJ. Nature 2009;458:746.